

Highly Efficient Perovskite Nanocrystal Light-Emitting Diodes Enabled by a Universal Crosslinking Method

Guangru Li, Florencia Wisnivesky Rocca Rivarola, Nathaniel J. L. K. Davis, Sai Bai, Tom C. Jellicoe, Francisco de la Peña, Shaocong Hou, Caterina Ducati, Feng Gao, Richard H. Friend, Neil C. Greenham,* and Zhi-Kuang Tan*

Metal-halide perovskite semiconductors have attracted significant research interest, due to a combination of low-cost solution processability and remarkable performance in optoelectronic devices.^[1,2] In 2014, we demonstrated infrared and visible electroluminescence in methylammonium lead halide perovskites, using a charge-confined diode structure to achieve effective radiative recombination.^[2–4] However, the use of methylammonium halide, which is a chemical combination of gaseous methylamine and hydrogen halide, necessarily limits the thermal stability of these perovskite devices. Replacing methylammonium with inorganic cesium offers the perovskite extra thermal stability up to its melting at ≈ 500 °C, but makes it more intractable toward solution processing.^[5] Recently, Protesescu et al. demonstrated the synthesis of cesium lead halide perovskite nanocrystals,^[6] following the traditional approaches of growing and stabilizing semiconductor particles in the

presence of aliphatic ligands.^[7] These perovskite nanocrystals are highly luminescent and emit over the full visible range, making them ideal candidates for luminescent display applications.^[6] The synthetic steps are generally straightforward, and the easy control of halide content allows the perovskite bandgaps to be tailored, both by chemical compositions as well as by quantum size effects. So far, perovskite nanocrystals are shown to have color-pure emission, close to unity photoluminescence yield and low lasing thresholds.^[8] These nanocrystals were also attempted in light-emitting devices, but efficiencies remain modest at 0.12%.^[9]

Here, we show the preparation of highly efficient perovskite light-emitting diodes (PeLED) using solution-processed nanocrystals. We apply a new trimethylaluminum (TMA) vapor-based crosslinking method to render the nanocrystal films insoluble, thereby allowing the deposition of subsequent charge-injection layers without the need for orthogonal solvents. The resulting near-complete nanocrystal film coverage, coupled with the natural confinement of injected charges within the perovskite crystals, facilitate electron–hole capture and give rise to a remarkable electroluminescence yield of 5.7%.

Figure 1a shows the device architecture of our perovskite nanocrystal light-emitting diode, and Figure 1b shows the energy-level diagram of the materials within the device stack. Here, our electron-injection layer comprises a film of zinc oxide (ZnO) nanocrystals, directly deposited on an indium tin oxide (ITO)-coated glass substrate.^[4] The cesium lead halide nanocrystals were solution-coated onto the ZnO film as the emissive layer. Due to the presence of aliphatic ligands on the nanocrystals, the perovskite film remains soluble to organic solvents, which limits the deposition of subsequent charge-injection layers using solution methods. We employed a new TMA vapor-phase crosslinking technique to fix the nanocrystal film in place, thereby enabling us to solution-cast a layer of TFB polymer (poly[(9,9-dioctylfluorenyl-2,7-diyl)-co-(4,4'-(N-(4-sec-butylphenyl)diphenylamine))] above without washing the nanocrystals off. TFB serves primarily as a hole-injection and electron-blocking layer. A thin, high work-function molybdenum trioxide (MoO₃) interlayer and silver electrode were vacuum-thermal evaporated to complete the device.

As shown in Figure 1c,d, our perovskite nanocrystal devices show saturated and color-pure emission. We control the perovskite bandgap, primarily by tailoring the halide composition, and achieve electroluminescence across a wide range of the visible spectrum. Our red, orange, green, and blue devices emit at wavelengths of 698, 619, 523, and 480 nm, respectively.

G. Li, N. J. L. K. Davis, T. C. Jellicoe, Prof. R. H. Friend, Prof. N. C. Greenham, Prof. Z.-K. Tan
Cavendish Laboratory
University of Cambridge
J.J. Thomson Avenue, Cambridge CB3 0HE, UK
E-mail: ncg11@cam.ac.uk; zkt20@cam.ac.uk, chmtanz@nus.edu.sg



F. Wisnivesky Rocca Rivarola, Dr. F. de la Peña, Prof. C. Ducati
Department of Materials Science and Metallurgy
University of Cambridge
Charles Babbage Road, Cambridge CB3 0FS, UK

S. Bai, Prof. F. Gao
Biomolecular and Organic Electronics
IFM

Linköping University
Linköping 58183, Sweden

Dr. S. Hou
Department of Engineering
University of Cambridge
J.J. Thomson Avenue, Cambridge CB3 0FA, UK

Prof. Z.-K. Tan
Department of Chemistry
National University of Singapore
3 Science Drive 3, S117543, Singapore

Prof. Z.-K. Tan
Solar Energy Research Institute of Singapore
National University of Singapore
7 Engineering Drive 1, S117574, Singapore

This is an open access article under the terms of the Creative Commons Attribution License, which permits use, distribution and reproduction in any medium, provided the original work is properly cited.

DOI: 10.1002/adma.201600064

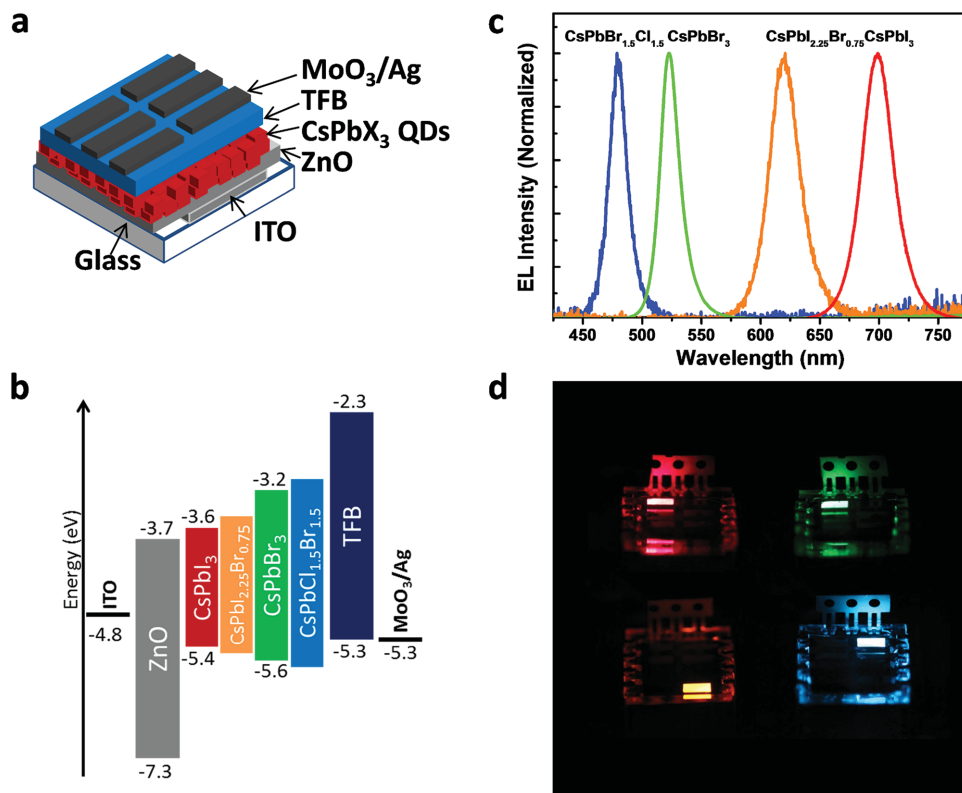


Figure 1. a) Perovskite nanocrystal light-emitting diode with an ITO/ZnO/CsPbX₃/TFB/MoO₃/Ag device architecture, where X represents I, Br, or Cl. b) Energy-level diagram showing the valence and conduction band levels of the materials in the device. Energy levels were estimated from literature values, without taking into account the quantum size effects.^[10] Bandgap energies were estimated from the EL emission peaks. c) Electroluminescence spectra of red-, orange-, green-, and blue-emitting perovskite nanocrystal LEDs. d) Images of perovskite nanocrystal LEDs in operation.

All devices exhibit narrow-width emission, with their full-width at half maxima (FWHM) in the range of 17–31 nm. The red and green LEDs were made, respectively, from the pure iodide and pure bromide perovskites, while the orange and blue LEDs were made from mixed-halide perovskites, with CsPbI_{2.25}Br_{0.75} and CsPbBr_{1.5}Cl_{1.5} compositions, respectively.

The crosslinking of the perovskite nanocrystals was critical toward the realization of our device structure. Traditionally, nanocrystals have been crosslinked, or made insoluble, using ligand exchange techniques, where shorter-chain bi-functionalized organic ligands (e.g., diamines or dithiols) were applied to replace the longer-chain oleyl ligands.^[11] However, the replacement with smaller ligands often creates cracks and gaps within the nanocrystal film, which could lead to electrical shunts and reduced device performance.^[12] Closer packing of the nanocrystals could also lead to the self-quenching of the nanocrystals and a lower photoluminescence yield,^[13] often caused by a more effective Förster resonant energy transfer (FRET) to non-radiative sites.^[14] Here, crosslinking is achieved by exposing the perovskite nanocrystal film to short pulses of TMA vapor within an enclosed vacuum chamber at room temperature, followed by standing the treated film in ambient air. This creates a well-connected network of hydroxide-terminated aluminum oxide that links the nanocrystals together, hence rendering them insoluble. This vapor-phase technique does not involve ligand exchange processes, and is therefore useful in crosslinking the nanocrystals without altering the original crystal arrangements,

thereby allowing much of the film's original structural and electronic properties to be preserved. The photoluminescence spectra of the nanocrystals also remain unchanged after the TMA treatment, hence confirming that the crosslinking has no effect on their optical bandgap. (Note that we use a slightly modified TMA treatment procedure for the blue-emitting nanocrystals—see Figure S1, Supporting Information.)

In order to investigate the effectiveness of crosslinking, we varied the exposure of the perovskite nanocrystals to different pulse durations of TMA vapor, and measured the nanocrystal retention upon washing with toluene. The crystal retention ratio was determined using UV–visible absorption spectroscopy. As shown in Figure 2a, the crosslinking was remarkably rapid even at room temperature, and a near complete retention of nanocrystals was achieved in less than 0.5 s of TMA exposure. The inset scanning electron microscopy (SEM) images show a significant wash-off for the non-crosslinked nanocrystals, while the TMA-treated nanocrystals were completely retained after washing. Detailed SEM images and large area scans of the nanocrystal films, upon washing with different organic solvents, are shown in Figure S2 (Supporting Information). Interestingly, we observe a corresponding increase in the photoluminescence quantum efficiency (PLQE) of CsPbI₃ and CsPbBr₃ with TMA treatment, but a decrease in the case of CsPbBr_{1.5}Cl_{1.5} (see Figure 2b). This PL enhancement is particularly remarkable for the CsPbI₃ nanocrystals, raising its PL by more than a factor of 3, from ≈25% in the untreated film to

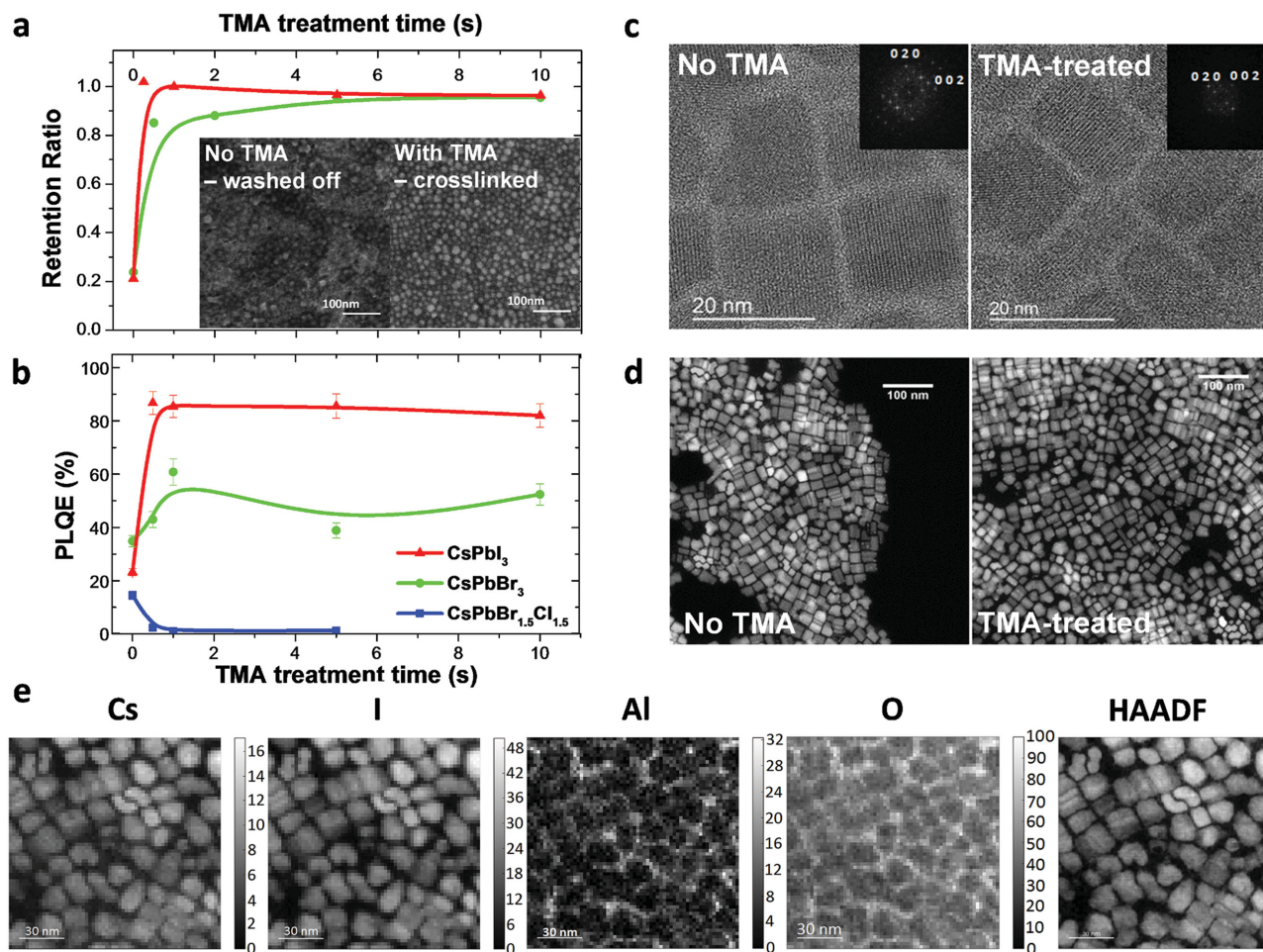


Figure 2. a) Retention ratio of TMA-treated and non-treated perovskite nanocrystal upon washing with toluene, plotted against the duration of TMA treatment. Inset images show the SEM images of washed off and crosslinked perovskite nanocrystals (CsPbI₃), upon washing with toluene. b) Photoluminescence quantum efficiency (PLQE) of perovskite nanocrystals, plotted against the duration of TMA crosslinking treatment. c) High-resolution TEM (HRTEM) images of untreated and TMA-treated CsPbI₃ nanocrystals. The insets show the fast Fourier transform (FFT) for the nanocrystals. Both samples were imaged on the [100] zone axis. d) High-angle annular dark-field scanning TEM (HAADF-STEM) images of untreated and TMA-treated CsPbI₃ nanocrystals, used for size-distribution analysis. e) Cesium, iodine, aluminum, and oxygen elemental maps obtained by quantitative analysis of an EELS spectrum image. The corresponding HAADF image is shown in the figure. Intensity units for EELS are arbitrary (same units for all maps) but proportional to the number of atoms in the volume traversed by the electron beam.

≈85% in the TMA-treated film. We note that this is possibly one of the highest PLQEs achieved in a non-core-shell structured nanocrystal thin film.

In an attempt to unravel the origins of the PL enhancement, we took high-resolution transmission electron microscopy (HRTEM) images (Figure 2c) and high-angle annular dark-field scanning TEM (HAADF-STEM) images (Figure 2d) of the CsPbI₃ perovskite nanocrystals before and after the TMA treatment, and further analyzed the distribution of main elements within the samples using electron energy loss spectroscopy (EELS) spectrum imaging (Figure 2e). The nanocrystals show an average size of 19 nm (see Figure S3, Supporting Information), which points to minimal quantum confinement in their electronic bandgap.^[6] We analyzed the spacing distribution between the nanocrystals in the HRTEM images, and found the average crystal spacing to increase from 1.6 to 1.9 nm upon TMA treatment. We note that a spacing of 1.6 nm between the

crystals represents ≈0.55 ligand attachment per unit cell of the perovskite lattice. The spacing distribution analysis is shown in Figure S3 (Supporting Information) and further TEM images of CsPbBr₃ perovskite nanocrystals are shown in Figure S4 (Supporting Information).

By analyzing the EELS spectrum image using a combination of principal component analysis (PCA), independent component analysis (ICA), and curve-fitting quantification, we were able to map out the distribution of elements, and precisely identify the higher concentrations of aluminum and oxygen elements within the sub-2 nm gaps between the perovskite nanocrystals (Figure 2e). This indicates that the TMA treatment has successfully created an alumina network that covers all areas surrounding and in-between the nanocrystals. The intercalation of alumina among the ligands, therefore, accounts for the small increase in the crystal spacing. While this 0.3 nm increase in spacing may lead to a smaller degree

of PL quenching by FRET, it is unlikely to fully account for the threefold enhancement in PL yield. The changes in PL are therefore likely to be chemical in nature, where the introduction of TMA chemically passivates the nanocrystal surface and leads to a reduction in PL-quenching defects.^[15] To further verify that the aluminum is incorporated between the crystal spacing and not just above the nanocrystal film, we measured the X-ray photoelectron spectra (XPS) of the sample as a function of film depth, and found aluminum to be quite evenly distributed throughout the entire nanocrystal film thickness (see XPS depth profile in Figure S5, Supporting Information).

To elucidate the chemical crosslinking mechanism, we measured the infrared (IR) transmittance spectra of the nanocrystal samples before and after the TMA treatment. For comparison, we also measured the IR spectra of the organic ligands, and plotted them on the same graph in Figure 3a. Three distinct changes could be observed in the IR spectra following the TMA treatment. i) A broad peak centered around 3450 cm^{-1} is produced in all the TMA-treated samples, signally the presence of O–H stretch. This confirms hydroxide surface terminations as expected for an AlO_x network, and the role of ambient water in the crosslinking process. ii) Another broad peak appears around 630 cm^{-1} , and this is characteristic of vibrational modes in alumina.^[16] iii) A strong and sharp band appears at 1576 cm^{-1} (for samples containing oleic acid), which can be assigned to weakened C=O stretching. This is particularly clear in the case of TMA-treated oleic acid. It is likely that the bonding of the carboxylate group to the strongly Lewis acidic aluminum causes the C=O bond to be weakened, thereby giving a lower than usual stretching frequency. Interestingly, the C=O stretching band does not appear in the pristine nanocrystal samples, but only emerges after TMA treatment. This is likely to be due to

the coordination of the carboxylate group to the nanocrystals, thereby diminishing its oscillator strength.

With this information, we propose a reaction mechanism for the cross-linking process as shown in Figure 3b. The introduction of TMA coordinates and reacts with the carboxylate and amino groups of the ligands, adjacent to the nanocrystals. The subsequent exposure to ambient moisture hydrolyzes the remaining methyl-aluminum to give a network of alumina and aluminum hydroxide that are covalently bonded to the ligands. It is likely that the alumina that is formed next to the crystal surface successfully passivates the surface defects, thereby enhancing the crystals' photoluminescence yield. The strongly reactive TMA appears to be benign toward the iodide and bromide perovskites, but causes some level of damage to the chloride perovskites, hence resulting in a degradation of PL in the latter. To further verify the role of ligands in this crosslinking process, we attempted to wash off TMA-treated oleic acid and oleylamine (i.e., no nanocrystals) with toluene. We show in Figure S6 (Supporting Information) that the ligands were crosslinked and insoluble upon TMA treatment, hence indicating that many of the ligands are chemically incorporated into the alumina network across the nanocrystal film. In order to prove the generality of our crosslinking technique, we treated thin films of CdSe and PbS nanocrystals with TMA, and demonstrate them to be insoluble to organic solvents upon treatment (see Figure S7, Supporting Information).

The TMA crosslinking method has enabled us to make high-performance light-emitting devices using these nanocrystalline lead halide perovskites. Figure 4a–d shows the detailed device characteristics of our perovskite nanocrystal LEDs. High luminance levels of 2335 and 1559 cd m^{-2} were achieved in our green and orange-emitting devices, respectively, at current densities

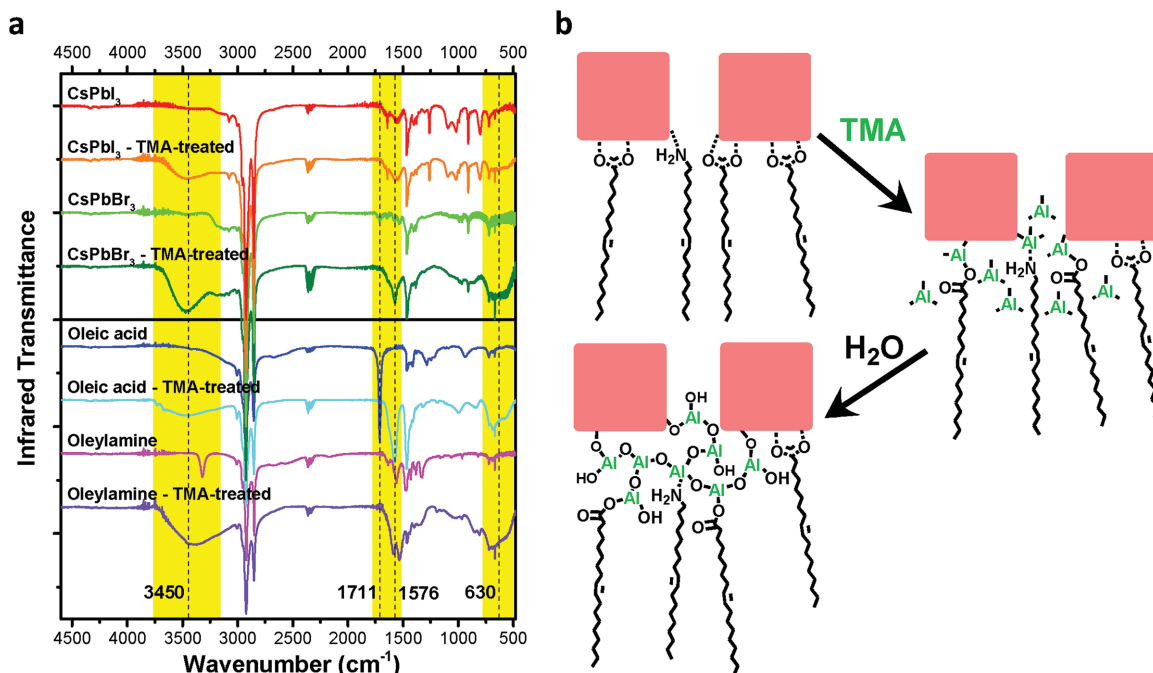


Figure 3. a) Fourier transform infrared (FTIR) spectra of perovskite nanocrystals and their ligands before and after TMA treatment. b) Reaction schematic of the TMA crosslinking process.

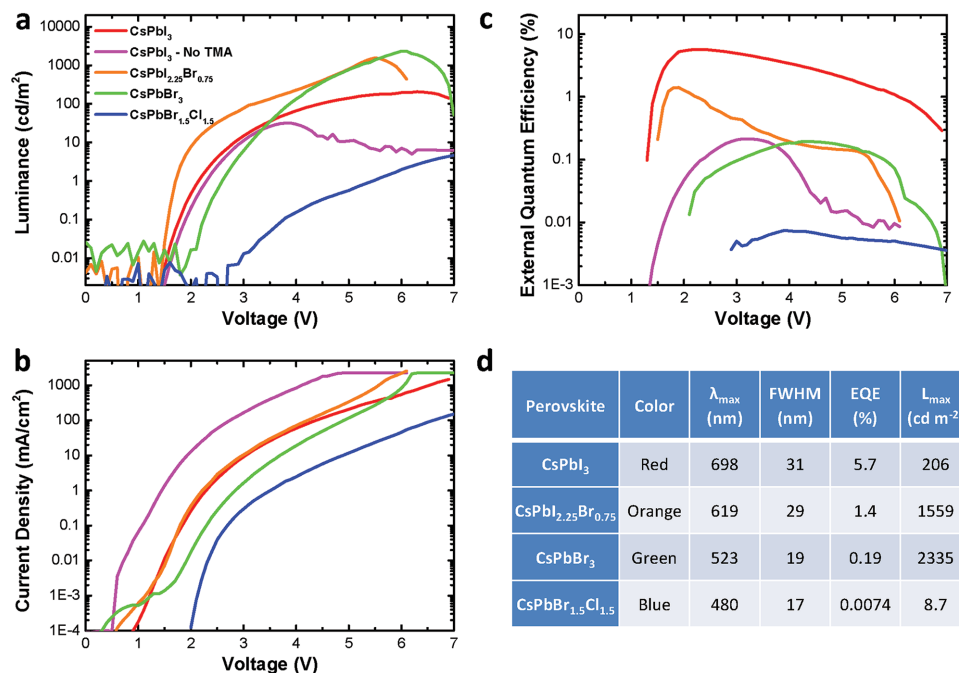


Figure 4. a) Luminance versus voltage plots of perovskite nanocrystal LEDs. b) Current density versus voltage plots of perovskite nanocrystal LEDs. c) External quantum efficiency versus voltage plots of perovskite nanocrystal LEDs. d) Table of summary of perovskite nanocrystal LED performance.

of 831 and 852 mA cm⁻². As shown in Figure 4b, charge injection turns on efficiently close to the bandgap voltage of the perovskite. To demonstrate the importance of our crosslinking method, we plotted the current–voltage characteristics of the non-TMA-treated CsPbI₃ device, and show that the current density is more than an order of magnitude higher than the crosslinked counterpart, even at similar or lower luminance levels. This is a clear indication of current leakage,^[3] which is a result of voids created from the wash-off of the perovskite nanocrystals.

We achieved remarkable external quantum efficiencies (EQE), as high as 5.7%, in the crosslinked red-emitting CsPbI₃ device, more than an order of magnitude higher than the non-crosslinked device (see Figure 4c) and a factor of 50 higher than the previous report.^[9] Correcting for out-coupling losses,^[17] this would be equivalent to an internal quantum efficiency of $\approx 26\%$. We note that our CsPbI₃ device emits at 698 nm, close to the edge of human-eye sensitivity, and therefore gives only a modest luminance level of 206 cd m⁻² at a current density of 755 mA cm⁻². We observed that the EQE of the nanocrystal devices decrease generally with the widening of the perovskite bandgap. This is in line with the trends of a lower PLQE in our green and blue-emitting materials (see Figure 2b). The less-ideal charge injection into larger bandgap perovskites could also result in the lower device efficiencies. Figure 4d gives a summary of the key performance parameters of our nanocrystal LEDs.

During our investigation of the mixed-halide perovskite nanocrystals (CsPbI_{2.25}Br_{0.75} and CsPbBr_{1.5}Cl_{1.5}), we noticed that their emission red-shifts reversibly during device operation, and return slowly toward their original state after resting (see Figure S8, Supporting Information). This emission shift is not observed in the pure-halide samples. This may be related to

previous observations on photoluminescence shifts in mixed-halide perovskites upon photoexcitation, which was suggested to be due to phase segregation into purer halide phases.^[18] We note that our films consist of spatially separated nanocrystals, and any phase segregation or halide rearrangements could therefore occur only within a small domain of less than 20 nm. We further show in Figure S9 (Supporting Information) that the EL shifts are completely consistent with the PL shifts, thereby confirming that these shifts are a result of intrinsic changes within the perovskites, and not due to a change in the device charge-injection properties during operation. In view of the emission shifts in mixed-halide systems, bandgap tuning of pure-halide perovskites via quantum size effect may emerge as the more successful strategy for consumer display applications, where stringent requirements on emission stability are demanded.

We have now successfully departed from the traditional core–shell nanocrystal approach, and shown that highly efficient electroluminescence could be realized in semiconductor nanocrystals using a simple TMA crosslinking technique. The remarkable ability of alumina to double as a surface passivating agent further makes the TMA treatment an attractive technique for the fabrication of quantum-dot optoelectronic devices. Indeed, given their intensely luminescent properties, versatile color tuning, coupled with an enhanced thermal stability, these all-inorganic lead halide perovskites may quickly emerge as strong contenders in the color display industry.

Experimental Section

Materials: TFB was provided by Cambridge Display Technology (CDT) and was used as received. All other chemicals were purchased from Sigma–Aldrich, and were used as received.

Synthesis of CsPbX₃ (X = Cl, Br, I) Nanocrystals: Perovskite nanocrystals were synthesized using previously reported procedures.^[6] Cs₂CO₃ (0.814 g, 99.9%) was loaded into 100 mL three-neck flask along with octadecene (ODE) (30 mL, 90%) and oleic acid (OA) (2.5 mL, 90%), and the mixture was dried for 2 h at 120 °C under N₂. The solution temperature was then lowered to 100 °C. ODE (75 mL), oleylamine (OLA) (7.5 mL, 90%), and dried OA (7.5 mL) and PbX₂ (2.82 mmol) such as PbI₂ (1.26 g, 99.99%), PbBr₂ (1.035 g, 99.99%), PbCl₂ (0.675 g, 99.99%), or their mixtures were loaded into a 250 mL three-neck flask and dried under vacuum for 2 h at 120 °C. After complete solubilization of the PbX₂ salt, the temperature was raised to 170 °C and the Cs-oleate solution (6.0 mL, 0.125 M in ODE, prepared as described above) was quickly injected. After 10 s, the reaction mixture was cooled in an ice-water bath. For CsPbCl₃ synthesis, 1 mL of trioctylphosphine (TOP) (97%) was added to solubilize PbCl₂. The nanocrystals were precipitated from solution by the addition of equal volume anhydrous butanol (BuOH) (99%) (ODE:BuOH = 1:1 by volume). After centrifugation, the supernatant was discarded and the nanocrystals were redispersed in anhydrous hexane (99%) and precipitated again with the addition of BuOH (hexane:BuOH = 1:1 by volume). These were redispersed in hexane. The nanocrystal dispersion was filtered through a 0.2 µm poly(tetrafluoroethylene) (PTFE) filter and diluted to 10 mg mL⁻¹ in hexane before use.

Synthesis of ZnO Nanocrystals: Colloidal ZnO nanocrystals were synthesized by a solution-precipitation process according to previously reported procedures.^[19] Typically, zinc acetate dihydrate (329 mg) was dissolved in dimethyl sulfoxide (DMSO) (0.5 M) by stirring at room temperature. A solution of tetramethylammonium hydroxide (TMAH) (453 mg) in ethanol (5 mL) was then added dropwise within 5 min. After 2 h, the product mixture was decanted and washed twice with ethyl acetate and ethanol. Ethanol (6 mL) was added to disperse the precipitate and produce a colloidal ZnO nanocrystal dispersion with a concentration of ≈7 mg mL⁻¹. The dispersion was filtered with a 0.45 µm PTFE filter before use.

Crosslinking of Perovskite Nanocrystals: A BENEQ TFS20 atomic layer deposition (ALD) system was used for the vapor-phase crosslinking treatment. High-purity TMA was purchased from SAFC Hitech. The deposition temperature was set at 18 ± 1 °C, which is also the typical ambient room temperature. The reactor chamber was pumped down below 0.2 mbar before starting the process. TMA was applied in short pulses at a partial pressure of ≈0.01 mbar. The dosage of TMA was controlled by varying the total length of TMA pulses between 0.25 and 20 s. The duration of each pulse was limited to 1 s, hence a 10 s dosage is, for instance, achieved with 10 × 1 s pulses.

LED Device Fabrication: A 7 mg mL⁻¹ dispersion of ZnO nanocrystals in ethanol was spin-coated onto an ITO-coated glass substrate at 1500 rpm for 30 s, followed by annealing at 100 °C for 10 min in a nitrogen-flushed glovebox to give a 15 nm film. A 10 mg mL⁻¹ perovskite nanocrystal dispersion in hexane was spin-coated at 1000–2000 rpm for 20 s in air to give a 30–50 nm film. The films were allowed to dry in air for ≈10 min, and were transferred into the ALD chamber for crosslinking treatment. Following the crosslinking step, a solution of TFB in toluene (10 mg mL⁻¹) was spin-coated on top of the perovskite nanocrystals at 2000 rpm for 30 s in the glovebox to give a 60 nm thin film. MoO₃ (5 nm) and Ag (80 nm) metal layers were deposited by thermal evaporation in a high vacuum of below 5 × 10⁻⁶ mbar. The devices were encapsulated by UV-epoxy.

LED Characterization: Current versus voltage characteristics were measured using a Keithley 2400 source measure unit. The photon flux was measured simultaneously using a calibrated silicon photodiode centered over the light-emitting pixel. Luminance in cd m⁻² was calculated based on the emission spectrum of the LED, weighted against the standard luminosity function and on the known spectral response of the silicon photodiode. The external quantum efficiency was calculated assuming a Lambertian emission profile. Electroluminescence spectra were measured using a Labsphere CDS-610 spectrometer.

Optical Characterization: In the PL measurements, the nanocrystal films were placed in a nitrogen-flushed integrating sphere and were

photoexcited using a 405 nm continuous-wave laser (1.5 mW). The laser and the emission signals were measured and quantified using a calibrated Andor iDus DU490A InGaAs detector for the determination of PL quantum efficiency. UV–visible absorption of the nanocrystal films was measured using an HP 8453 spectrometer. Samples were prepared on fused-silica substrate, using same processing parameters as in device fabrication.

FTIR Measurements: Mid-IR FTIR data were measured by an Agilent Technologies Cary 600 Series FTIR spectrometer. Nanocrystals were spin-coated onto a KBr substrate, and measured in the wavenumber range of 5000–500 cm⁻¹.

Electron Microscopy: TEM characterization was carried out on close-packed CsPbI₃ and CsPbBr₃ nanocrystals that were drop-cast on thin TEM carbon grids. The TEM samples were analyzed in an FEI Tecnai Osiris TEM/STEM 80-200 microscope operated at 200 kV. The HAADF-STEM images were acquired using a Fischione detector. The EELS spectra were acquired using a Gatan Enfium ER 977 spectrometer equipped with DualEELS. Core-loss and low-loss spectra were acquired quasi-simultaneously over different regions of the specimen, using a 2 nm pixel size and a dispersion of 1 eV per channel. The dwell time was 0.2 s for core-loss spectra and 10 µs for low-loss spectra. Convergence and collection angles were 8.5 and 34 mrad, respectively. The elemental maps were obtained by weighted PCA and ICA.^[20] The quantification by curve fitting of the ICA results was performed using Hartree–Slater cross sections. All the EELS analysis was performed using the open source software package HyperSpy.^[21] SEM images were acquired using the in-lens detector in a LEO 1550 system. The acceleration voltage was set at 10 kV.

Supporting Information

Supporting Information is available from the Wiley Online Library or from the author.

Acknowledgements

This work was supported by the EPSRC [Grant Nos. EP/M005143/1, EP/J017361/1, and EP/G037221/1]. G.L. thanks Gates Cambridge Trust for funding. F.W.R.R. is grateful for financial support from CNPq [Grant No. 246050/2012-8]. N.J.L.K.D. thanks the Cambridge Commonwealth European and International Trust, Cambridge Australian Scholarships and Mr. Charles K. Allen for financial support. F.W.R.R., F.D.P., and C.D. acknowledge funding from the ERC under Grant No. 259619 PHOTO-EM. C.D. acknowledges financial support from the EU under Grant No. 312483 ESTEEM2. F.G. acknowledges financial support from the Swedish Government Strategic Research Area in Materials Science on Functional Materials at Linköping University (Faculty Grant SFO Mat LiU No 200900971). The data underlying this publication are available at <https://www.repository.cam.ac.uk/handle/1810/253968>.

Note: The presentation of the author name F. Wisnivesky Rocca Rivarola was corrected on May 6, 2016 after initial publication online.

Received: January 6, 2016

Revised: February 1, 2016

Published online: March 16, 2016

- [1] a) A. Kojima, K. Teshima, Y. Shirai, T. Miyasaka, *J. Am. Chem. Soc.* **2009**, *131*, 6050; b) M. M. Lee, J. Teuscher, T. Miyasaka, T. N. Murakami, H. J. Snaith, *Science* **2012**, *338*, 643; c) J. Burschka, N. Pellet, S.-J. Moon, R. Humphry-Baker, P. Gao, M. K. Nazeeruddin, M. Gratzel, *Nature* **2013**, *499*, 316.

- [2] Z.-K. Tan, R. S. Moghaddam, M. L. Lai, P. Docampo, R. Higler, F. Deschler, M. Price, A. Sadhanala, L. M. Pazos, D. Credgington,

- F. Hanusch, T. Bein, H. J. Snaith, R. H. Friend, *Nat. Nanotechnol.* **2014**, *9*, 687.
- [3] R. L. Hoye, M. R. Chua, K. P. Musselman, G. Li, M. L. Lai, Z. K. Tan, N. C. Greenham, J. L. MacManus-Driscoll, R. H. Friend, D. Credgington, *Adv. Mater.* **2015**, *27*, 1414.
- [4] J. Wang, N. Wang, Y. Jin, J. Si, Z. K. Tan, H. Du, L. Cheng, X. Dai, S. Bai, H. He, Z. Ye, M. L. Lai, R. H. Friend, W. Huang, *Adv. Mater.* **2015**, *27*, 2311.
- [5] C. C. Stoumpos, C. D. Malliakas, J. A. Peters, Z. Liu, M. Sebastian, J. Im, T. C. Chasapis, A. C. Wibowo, D. Y. Chung, A. J. Freeman, B. W. Wessels, M. G. Kanatzidis, *Cryst. Growth Des.* **2013**, *13*, 2722.
- [6] L. Protesescu, S. Yakunin, M. I. Bodnarchuk, F. Krieg, R. Caputo, C. H. Hendon, R. X. Yang, A. Walsh, M. V. Kovalenko, *Nano Lett.* **2015**, *15*, 3692.
- [7] a) M. L. Steigerwald, A. P. Alivisatos, J. M. Gibson, T. D. Harris, R. Kortan, A. J. Muller, A. M. Thayer, T. M. Duncan, D. C. Douglass, L. E. Brus, *J. Am. Chem. Soc.* **1988**, *110*, 3046; b) C. B. Murray, D. J. Norris, M. G. Bawendi, *J. Am. Chem. Soc.* **1993**, *115*, 8706; c) V. L. Colvin, M. C. Schlamp, A. P. Alivisatos, *Nature* **1994**, *370*, 354.
- [8] S. Yakunin, L. Protesescu, F. Krieg, M. I. Bodnarchuk, G. Nedelcu, M. Humer, G. De Luca, M. Fiebig, W. Heiss, M. V. Kovalenko, *Nat. Commun.* **2015**, *6*, 8056.
- [9] J. Song, J. Li, X. Li, L. Xu, Y. Dong, H. Zeng, *Adv. Mater.* **2015**, *27*, 7162.
- [10] a) J. H. Noh, S. H. Im, J. H. Heo, T. N. Mandal, S. I. Seok, *Nano Lett.* **2013**, *13*, 1764; b) J. Hwang, E.-G. Kim, J. Liu, J.-L. Brédas, A. Duggal, A. Kahn, *J. Phys. Chem. C* **2007**, *111*, 1378.
- [11] a) K.-S. Cho, E. K. Lee, W.-J. Joo, E. Jang, T.-H. Kim, S. J. Lee, S.-J. Kwon, J. Y. Han, B.-K. Kim, B. L. Choi, J. M. Kim, *Nat. Photonics* **2009**, *3*, 341; b) B. Ehrler, B. J. Walker, M. L. Böhm, M. W. B. Wilson, Y. Vaynzof, R. H. Friend, N. C. Greenham, *Nat. Commun.* **2012**, *3*, 1019.
- [12] J. Tang, K. W. Kemp, S. Hoogland, K. S. Jeong, H. Liu, L. Levina, M. Furukawa, X. Wang, R. Debnath, D. Cha, K. W. Chou, A. Fischer, A. Amassian, J. B. Asbury, E. H. Sargent, *Nat. Mater.* **2011**, *10*, 765.
- [13] T.-W. F. Chang, A. Maria, P. W. Cyr, V. Sukhovatkin, L. Levina, E. H. Sargent, *Synth. Met.* **2005**, *148*, 257.
- [14] C. R. Kagan, C. B. Murray, M. Nirmal, M. G. Bawendi, *Phys. Rev. Lett.* **1996**, *76*, 1517.
- [15] D. A. R. Barkhouse, A. G. Pattantyus-Abraham, L. Levina, E. H. Sargent, *ACS Nano* **2008**, *2*, 2356.
- [16] P. Tarte, *Spectrochim. Acta, Part A* **1967**, *23*, 2127.
- [17] N. C. Greenham, R. H. Friend, D. D. C. Bradley, *Adv. Mater.* **1994**, *6*, 491.
- [18] E. T. Hoke, D. J. Slotcavage, E. R. Dohner, A. R. Bowring, H. I. Karunadasa, M. D. McGehee, *Chem. Sci.* **2015**, *6*, 613.
- [19] S. Bai, Z. Wu, X. Wu, Y. Jin, N. Zhao, Z. Chen, Q. Mei, X. Wang, Z. Ye, T. Song, R. Liu, S.-T. Lee, B. Sun, *Nano Res.* **2014**, *7*, 1749.
- [20] F. de la Peña, M. H. Berger, J. F. Hochepped, F. Dynys, O. Stephan, M. Walls, *Ultramicroscopy* **2011**, *111*, 169.
- [21] F. de la Peña, P. Burdet, T. Ostasevicius, M. Sarahan, M. Nord, V. T. Fauske, J. Taillon, A. Eljarrat, S. Mazzucco, G. Donval, L. F. Zagonel, M. Walls, I. Iyengar, *Hyperspy* **2015**, DOI:10.5281/zenodo.28025.